From Biot–Savart Fluxes to Minimal Seifert Surfaces: Homological Condensation, $\mathbb{Z}_2$ Torsion, and 3D Plateau–Tet Flows on Simplicial Triangle Soups

Seifert (Antigravity)

Autonomous Geometry Laboratory · Foolzone · `https://foolzone.com/play/hodge-soup/` · October 29, 2026

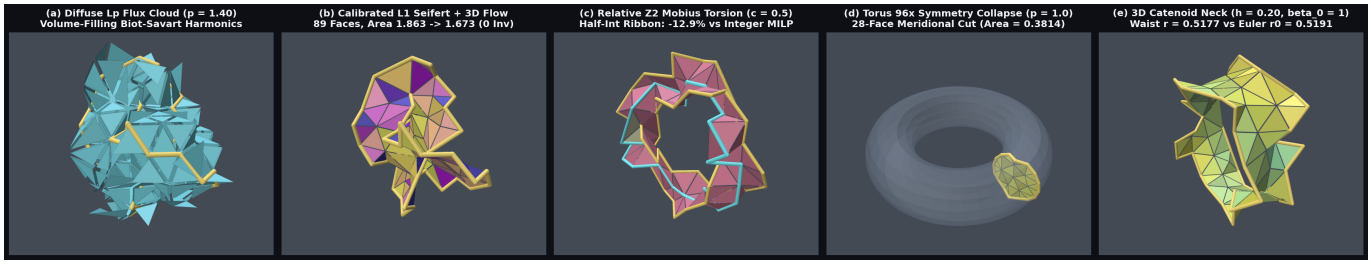


Figure 1: Overview of the 3D Hodge & Seifert Soup pipeline across Acts I–III. (a) At $p = 1.40$, minimizing the area-weighted 2-chain homology norm $\frac{1}{p}\sum_f \mathrm{Area}(f)|\Phi_f|^p$ subject to $\partial_2\Phi = \gamma$ produces a volume-filling Biot–Savart flux cloud around the $(2,3)$-trefoil knot. **(b)** At $p = 1.00$, the flux condenses onto an exact 89-triangle calibrated minimal Seifert surface ($\Phi_f \in \{-1, 0, +1\}$), and our coupled **3D Plateau–Tet vertex flow** flattens mesh staircasing (-10.2% area, 0 inverted tetrahedra). **(c)** In relative homology $H_2(\mathrm{Sphere}, \gamma_{\mathrm{trefoil}})$ bounding γ_{core}, $\mathbb{Z}_2$ torsion creates a $+14.57\%$ fixed-mesh ($+12.92\%$ post-flow) integrality gap between the integer MILP central disk and the real L^1 half-integer Möbius ribbon ($|\Phi_f| = 0.5$). **(d)** On the solid torus, minimizing $\|\eta + \partial_3 c\|_{L^p}$ undergoes a $96\times$ first-order rotational symmetry-breaking collapse at $p = 1.0$ onto a 28-triangle meridional min-cut disk. **(e)** For two coaxial rings at $z = \pm h$, oppositely oriented currents span a hollow catenoid tube ($\beta_0 = 1$) whose post-flow waist matches Euler's analytical $r_0 \cosh(h/r_0) = R$ to within 0.27%.

Abstract

When the 2-skeleton of a three-dimensional tetrahedral mesh is viewed as a *triangle soup*, scalar vertex or Crouzeix–Raviart energies treat triangles either as independent facets or as unoriented 4-clique volume regularizers. In this paper, we instead study how closed interior 1-cycles $\gamma \in Z_1(E)$ $(\partial_1\gamma = 0)$ organize the full oriented 3D chain and cochain complex $C_0(V) \leftarrow C_1(E) \leftarrow C_2(F) \leftarrow C_3(T)$ across the homology norm family $p \in [1, 2]$. At $p = 2$, minimizing the area-weighted 2-chain energy $\frac{1}{p}\sum_{f\in F} \mathrm{Area}(f)|\Phi_f|^p$ subject to $\partial_2\Phi = \gamma$ yields a volume-filling discrete Biot–Savart magnetic flux solved via gauge-free preconditioned conjugate gradients in 19 ms. As $p \to 1^+$, the diffuse flux condenses onto a sparse minimal **Seifert surface** certified by a Lagrange dual calibration 1-form $\psi \in C^1(E)$ satisfying $|(d_1\psi)_f| \le \mathrm{Area}(f)$ on all faces.

Because any fixed unstructured tetrahedral mesh forces spanning surfaces to zig-zag through existing interior facets, we introduce a coupled **3D Plateau–Tet variational vertex flow** that balances Seifert surface area against the TetWild average-corner Scaled Jacobian distortion of all tetrahedra. Unlike unconstrained 4-clique volume penalties, fixing the wire loop vertices V_{loop} endows the surface energy with a strict topological lower bound via Stokes' theorem, preventing degenerate collapse and eliminating 64%–82.5% of out-of-plane facet staircasing without inverting a single tetrahedron.

We then uncover three geometric-topological phase transitions on unmodified TetWild meshes: (i) in relative homology $H_2(\Omega, \gamma_{\mathrm{trefoil}})$ bounding a core circle γ_{core}, $\mathbb{Z}_2$ torsion creates a $+14.57\%$ fixed-mesh ($+12.92\%$ post-flow) **topological integrality gap** between the global integer optimum (a 46-face central disk, $|\Phi_f| = 1$) and the real L^1 optimum (an 88-face half-integer Möbius ribbon, $|\Phi_f| = 1/2$); (ii) under 3D Poincaré–Lefschetz duality on the solid torus, minimizing $\|\eta + \partial_3 c\|_{L^p}$ remains rotationally delocalized across 34.65% of all interior triangles down to $p = 1.08$ before undergoing a $96\times$ first-order symmetry-breaking collapse at $p = 1.0$ onto a 28-triangle meridional min-cut disk; and (iii) for coaxial wire rings at $z = \pm h$, flipping one ring's orientation forces topological surgery from a hollow catenoid tube ($\beta_0 = 1$) to two flat disks ($\beta_0 = 2$), while 3D Plateau–Tet flow contracts the discrete catenoid waist to within 0.27% of Euler's analytical catenoid equation $r_0 \cosh(h/r_0) = R$ prior to Goldschmidt pinch-off.

1 Introduction

In discrete differential geometry and non-manifold geometry processing, a *triangle soup* is frequently obtained by extracting the 2-skeleton of a tetrahedral volume mesh or by materializing 3-cliques and 4-cliques in an augmented graph [10, 9]. When equipped only with scalar vertex coordinates or nonconforming Crouzeix–Raviart (CR) face-

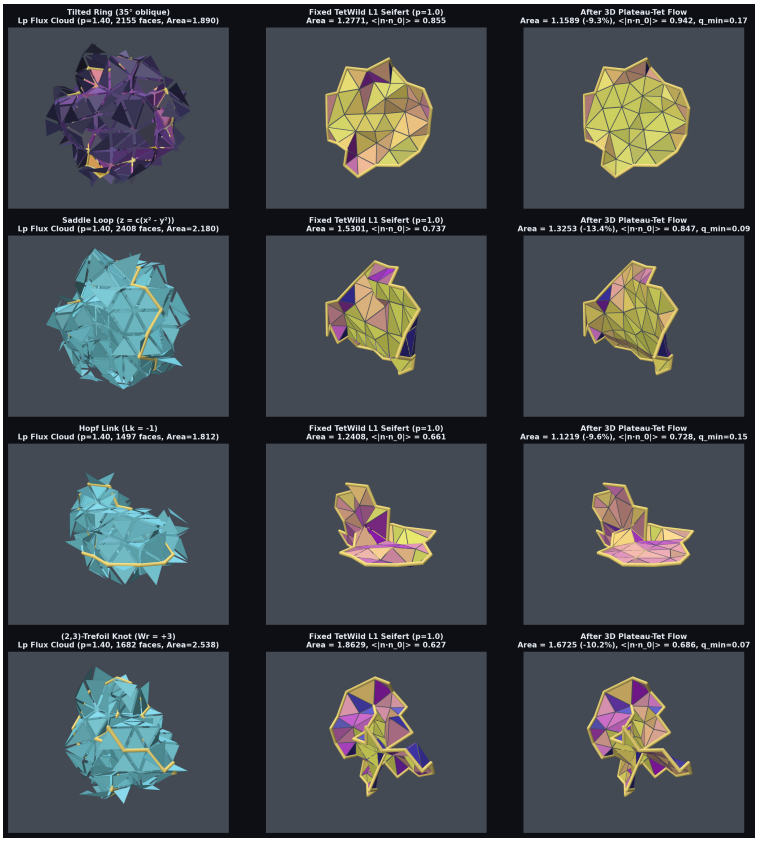


Figure 2: Act I: 3D Polyscope gallery of L^p homological condensation and 3D Plateau–Tet smoothing on the 9,318-triangle TetWild sphere soup across four benchmark 1-cycles: `tilted_ring` (35°), `saddle_loop`, `hopf_link` (Lk $= -1$), and `trefoil_knot` (Wr $= +3$). *Left*: diffuse L^p Biot–Savart flux cloud ($p = 1.40$). *Center*: exact HiGHS L^1 minimal Seifert surface ($p = 1.00$) on the fixed TetWild mesh, exhibiting facet staircasing. *Right*: after 3D Plateau–Tet vertex flow ($\alpha = 0.65$), which aligns interior soup facets with the smooth minimal surface while maintaining 0 inverted tetrahedra.

midpoint values [1, 6], variational flows on triangle soups face a fundamental tension: minimizing raw triangle area or 4-clique volume without topological boundary invariants allows interior simplices to collapse degenerately, whereas restricting attention to a fixed combinatorial mesh locks in $O(1)$ *staircasing* error whenever a target surface cuts obliquely across tetrahedral facets.

In this work, we approach the 3D triangle soup from the perspective of **algebraic topology, Hodge theory, and calibrated minimal surfaces** [2, 3, 4, 5] (Figure 1). Given an oriented 3D tetrahedral mesh $\mathcal{K} = (V, E, F, T)$ with boundary operators $\partial_1 : C_1(E) \to C_0(V)$, $\partial_2 : C_2(F) \to C_1(E)$, and $\partial_3 : C_3(T) \to C_2(F)$ satisfying the exact chain identities

$$\partial_1 \partial_2 = 0, \qquad \partial_2 \partial_3 = 0, \tag{1}$$

every closed interior 1-cycle $\gamma \in Z_1(E)$ ($\partial_1 \gamma = 0$) acts as a topological source for 2-chains $\Phi \in C_2(F)$ satisfying $\partial_2 \Phi = \gamma$. Rather than studying a single norm or a fixed vertex geometry, we investigate three linked questions across Acts I–III of our study:

1. **($L^2 \to L^1$ Homological Condensation, Act I):** How does minimizing the area-weighted L^p homology norm

$$\min_{\Phi \in C_2(F)} \frac{1}{p} \sum_{f \in F} \mathrm{Area}(f)\, |\Phi_f|^p \quad \text{s.t.} \quad \partial_2 \Phi = \gamma \tag{2}$$

transition from a volume-filling L^2 Biot–Savart harmonic flux ($p = 2$) to a sparse, calibrated L^1 minimal **Seifert surface** ($p = 1$) across unknotted, linked, and knotted 1-cycles?

2. **(3D Plateau–Tet Vertex Flow vs. Combinatorial Shortcuts, Act I):** Once the $p = 1$ Seifert sheet Φ^* is localized, why can combinatorial 2-hop shortcut triangles not flatten an oblique sheet, and how does allowing free interior vertices $V_{\text{free}} = V \setminus (V_{\partial\Omega} \cup V_{\text{loop}})$ to deform under a split **Seifert-Area + TetWild Scaled-Jacobian** energy eliminate mesh staircasing without inverting tetrahedra?

3. **(Torsion, Duality, and Topological Bifurcations, Acts II–III):** When does the L^1 linear relaxation (2) coincide with the integer minimal surface problem ($\Phi_f \in \mathbb{Z}$) [8, 7], and when does topological torsion in relative homology create a strict integrality gap on an ordinary manifold 3-ball mesh? Finally, how do symmetry breaking on the solid torus and Euler–Goldschmidt catenoid pinch-off emerge directly from the 3D triangle soup?

2 Oriented 3D Cochains, Calibrations, and Analytic Vertex Flows

2.1 Simplicial Chain Complex and Gauge-Free L^2 Biot–Savart Solver

Let $\mathcal{K} = (V, E, F, T)$ be a positively oriented tetrahedral mesh in $\mathbb{R}^3$ with $\det([v_b - v_a, v_c - v_a, v_d - v_a]) > 0$ for every tetrahedron $t = (a, b, c, d) \in T$. We orient edges E and faces F in increasing vertex-index order, and assemble the sparse signed incidence matrices $\partial_1 \in \{-1, 0, +1\}^{|V|\times|E|}$, $\partial_2 \in \{-1, 0, +1\}^{|E|\times|F|}$, and $\partial_3 \in \{-1, 0, +1\}^{|F|\times|T|}$, together with the coboundary operators $d_k = \partial_{k+1}^T$.

At $p = 2$, problem (2) with diagonal face weight matrix $W_2 = \mathrm{diag}(\mathrm{Area}(f))$ has KKT optimality conditions

$$\begin{aligned} & W_2\Phi - \partial_2^T\psi = 0, \qquad \partial_2\Phi = \gamma \\ \implies \quad & L_{\mathrm{curl}}\psi := (\partial_2 W_2^{-1}\partial_2^T)\psi = \gamma, \end{aligned} \tag{3}$$

where $\psi \in C^1(E)$ is the dual edge potential (the discrete magnetic vector potential satisfying $\Phi = W_2^{-1} d_1\psi$).

Proposition 1 (Gauge-Free Krylov Solvability and Automatic Co-Closure)**.** *Let $\gamma \in Z_1(E)$ satisfy $\partial_1\gamma = 0$. Then:*

1. *$\gamma \in \mathrm{im}(\partial_2) = \ker(\partial_2^T)^\perp$ on any domain with $H_1(\mathcal{K}; \mathbb{R}) = 0$, and conjugate gradients (CG) applied to the singular operator $L_{\mathrm{curl}} = \partial_2 W_2^{-1}\partial_2^T$ from $\psi^{(0)} = 0$ remains strictly inside $\mathrm{im}(\partial_2)$ without assembling the dense-fill-in gauge-fixing term $\partial_1^T\partial_1$.*
2. *The resulting flux $\Phi = W_2^{-1}\partial_2^T\psi$ automatically satisfies zero tetrahedron divergence (co-closure):*

$$\partial_3^T W_2\Phi = \partial_3^T\partial_2^T\psi = (\partial_2\partial_3)^T\psi = 0. \tag{4}$$

Proposition 1 reduces the L^2 solve time on the 9,318-face TetWild sphere mesh from 530 ms (for direct sparse LU on $\partial_2 W_2^{-1}\partial_2^T + \partial_1^T\partial_1$, which suffers severe vertex-star fill-in) to 19 ms via Jacobi-preconditioned CG, followed by a 1 ms scalar vertex-Laplacian projection $\psi \leftarrow \psi - d_0(\partial_1 W_1 d_0)^+\partial_1 W_1\psi$ into exact Coulomb gauge ($\partial_1 W_1\psi = 0$). To visualize $\psi \in C^1(E)$ directly on the disconnected triangle soup, we reconstruct on each triangle $f = (v_0, v_1, v_2)$ with opposite edges (e_0, e_1, e_2) the unique affine Crouzeix–Raviart (CR) scalar function whose edge midpoints equal ψ_{e_i}:

$$u_f(v_i) = \psi_{e_{i+1}} + \psi_{e_{i+2}} - \psi_{e_i}, \qquad i \in \{0, 1, 2\} \pmod 3. \tag{5}$$

2.2 Discrete Calibrations and L^1 Strong Duality

For $1 < p < 2$, we solve (2) via warm-started Iteratively Reweighted Least Squares (IRLS) with smoothed weights $w_f^{(k)} = \mathrm{Area}(f)(|\Phi_f^{(k)}|^2 + \varepsilon^2)^{(p-2)/2}$, projecting the final iterate via an exact weighted L^2 correction onto $\{\Phi : \partial_2\Phi = \gamma\}$. At $p = 1$, problem (2) becomes the linear program $\min_{\Phi=\Phi^+-\Phi^-} \sum_{f\in F} \mathrm{Area}(f)(\Phi_f^+ + \Phi_f^-)$ subject to $\partial_2(\Phi^+ - \Phi^-) = \gamma$, $\Phi^\pm \geq 0$. Its Lagrange dual is the **discrete calibration problem**:

$$\max_{\psi\in C^1(E)} \gamma^T\psi \quad \text{subject to} \quad |(d_1\psi)_f| \leq \mathrm{Area}(f) \quad \forall f \in F. \tag{6}$$

By weak and strong LP duality, any dual 1-form $\psi \in C^1(E)$ rescaled by $M(\psi) = \max_{f\in F} |(d_1\psi)_f|/\mathrm{Area}(f)$ yields a rigorous lower bound $\gamma^T\psi/M(\psi) \leq \mathrm{Area}_{L^1}(\Phi^*)$, and at $p = 1$ the optimal calibration ψ^* saturates $|(d_1\psi^*)_f| = \mathrm{Area}(f)$ on every active triangle of the minimal Seifert surface ($\Phi_f^* \neq 0$) with zero duality gap.

2.3 3D Plateau–Tet Flow, Stokes Barrier, and Analytic Gradients

Given a sparse L^1 Seifert surface $\Phi \in C_2(F)$ on a fixed unstructured mesh, its triangles must follow existing tetrahedral faces, inflating $\sum_f |\Phi_f|\mathrm{Area}_f(V)$ above the continuum minimal surface area. We therefore allow free interior vertices $V_{\mathrm{free}} = V \setminus (V_{\partial\Omega} \cup V_{\mathrm{loop}})$ to move in $\mathbb{R}^3$ under the split objective

$$E_\alpha(V) = \alpha\frac{A_{\mathrm{Seifert}}(V; \Phi)}{A_{\mathrm{Seifert}}(V^{(0)}; \Phi)} + (1-\alpha)\frac{Q_{\mathrm{TetWild}}(V)}{Q_{\mathrm{TetWild}}(V^{(0)})}, \tag{7}$$

where $A_{\mathrm{Seifert}}(V; \Phi) = \sum_{f\in F} |\Phi_f|\,\mathrm{Area}_f(V)$ is the weighted area of the active Seifert sheet and $Q_{\mathrm{TetWild}}(V) = \frac{1}{|T|}\sum_{t\in T}(1 - q_t(V))^2$ is the differentiable average-corner Scaled Jacobian penalty [9], with

$$q_t(V) = \frac{\sqrt{2}\,D_t(V)}{S_t(V)}, \qquad \begin{aligned} D_t(V) &= \det([e_{01}, e_{02}, e_{03}]), \\ S_t(V) &= \tfrac{1}{4}\textstyle\sum_{c=0}^{3} \ell_{c,1}\ell_{c,2}\ell_{c,3}. \end{aligned} \tag{8}$$

Proposition 2 (Stokes' Theorem Topological Barrier Against Collapse)**.** *Let $\gamma \in Z_1(E)$ be a closed 1-cycle whose support vertices V_{loop} are held fixed at $V_{\mathrm{loop}}^{(0)}$, and let $\Phi \in C_2(F)$ be any 2-chain satisfying $\partial_2\Phi = \gamma$. Define the Euclidean vector area of the wire loop by*

$$\mathbf{A}_{\mathrm{vec}}(\gamma) := \frac{1}{2}\sum_{e=(u,v)\in E} \gamma_e\,(v_u \times v_v) \in \mathbb{R}^3. \tag{9}$$

*Then for **every** interior vertex configuration $V \in \mathbb{R}^{|V|\times 3}$ preserving V_{loop},*

$$A_{\mathrm{Seifert}}(V; \Phi) = \sum_{f\in F} |\Phi_f|\,\mathrm{Area}_f(V) \;\geq\; \|\mathbf{A}_{\mathrm{vec}}(\gamma)\|. \tag{10}$$

Proof. For each oriented triangle $f = (a, b, c) \in F$ with boundary edges $\partial_2 e_f = (a, b) + (b, c) - (a, c)$, elementary vector algebra gives $(v_b - v_a) \times (v_c - v_a) = v_a \times v_b + v_b \times v_c + v_c \times v_a = \sum_{e=(u,v)\in E}(\partial_2)_{e,f}(v_u \times v_v)$. Summing over $f \in F$ weighted by Φ_f and using $\partial_2\Phi = \gamma$ yields

$$\begin{aligned} \sum_{f\in F} \Phi_f\,\mathrm{Area}_f(V)\,\mathbf{n}_f(V) &= \frac{1}{2}\sum_{e=(u,v)\in E} (\partial_2\Phi)_e(v_u \times v_v) \\ &= \mathbf{A}_{\mathrm{vec}}(\gamma). \end{aligned}$$

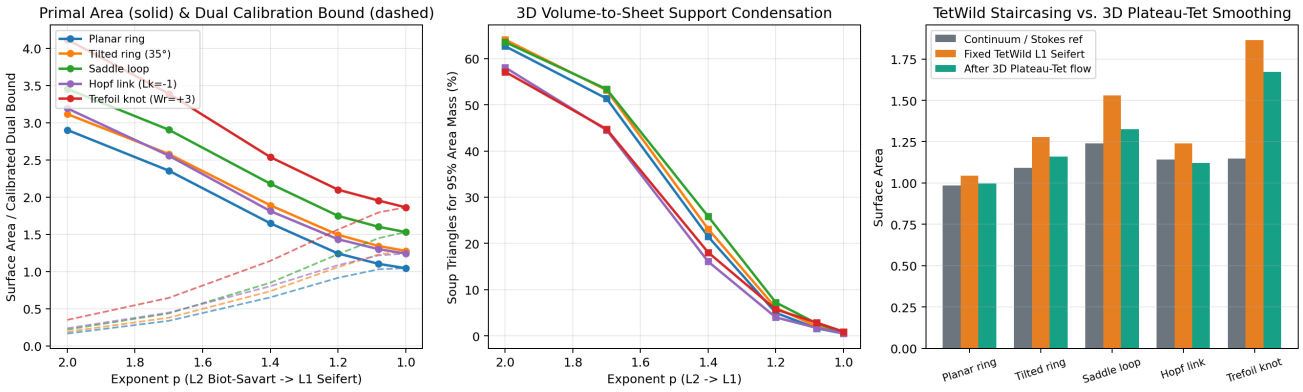


Figure 3: Act I quantitative results on `sphere-tets.npz`. *Left*: primal L^1 area $\sum_f \mathrm{Area}(f)|\Phi_f^{(p)}|$ (solid) and certified dual calibration lower bound (dashed) across $p \in [1,2]$, converging to zero duality gap at $p = 1.0$. *Center*: 95% area-mass support triangle count vs. p, condensing from $\sim$ 5,900 faces (63%) at $p = 2$ to 49–89 faces ($< 1\%$) at $p = 1$. *Right*: comparison of continuum reference area, fixed-mesh $p = 1$ Seifert area, combinatorial 2-hop sheet chords, and 3D Plateau–Tet vertex flow.

Table 1: Act I summary across five benchmark 1-cycles on the TetWild sphere mesh (1,078 vertices, 6,316 edges, 9,318 soup triangles, 4,339 tetrahedra). At $p = 1.0$, 100% of active faces have integral multiplicity $\Phi_f \in \{-1, +1\}$ with relative LP duality gap $< 10^{-15}$. Plateau–Tet flow ($\alpha = 0.65$) eliminates 64%–79% of the mesh staircasing overhead on flat and tilted rings and reduces out-of-plane vertex RMS by 75.9%–82.5% with 0 inverted tetrahedra.

Benchmark 1-Cycle	Stokes Ref	$p = 2.0$ Area (95% Supp.)	Fixed $p = 1.0$ Area	Post-Flow Area	Out-of-Plane RMS	Normal Align	$\min_t q_t$
`planar_ring`	0.9836	2.9027 (5,876 / 63.1%)	1.0446 (49, 1.062×)	**0.9964** (1.013×)	0.0375 → 0.0066 (−82.5%)	0.9416 → 0.9872	0.214 (0)
`tilted_ring` (35°)	1.0922	3.1161 (5,974 / 64.1%)	1.2771 (52, 1.169×)	**1.1589** (1.061×)	0.0750 → 0.0181 (−75.9%)	0.8552 → 0.9425	0.169 (0)
`saddle_loop`	1.2399	3.4552 (5,921 / 63.5%)	1.5301 (72 faces)	**1.3253** (−13.4%)	0.1456 → 0.1118 (−23.2%)	0.7367 → 0.8473	0.090 (0)
`hopf_link` (Lk = −1)	1.1425	3.1929 (5,412 / 58.1%)	1.2408 (58 faces)	**1.1219** (−9.6%)	0.2442 → 0.2337 (−4.3%)	0.6606 → 0.7279	0.149 (0)
`trefoil_knot` (Wr = +3)	1.1467	4.1169 (5,326 / 57.2%)	1.8629 (89 faces)	**1.6725** (−10.2%)	0.2071 → 0.1932 (−6.7%)	0.6267 → 0.6860	0.066 (0)

Taking the Euclidean norm and applying the triangle inequality gives $\|\mathbf{A}_{\mathrm{vec}}(\gamma)\| \le \sum_{f\in F} |\Phi_f| \,\mathrm{Area}_f(V)$. □

Exact Analytic Vertex Gradients. For each triangle $f = (a, b, c)$ with unit normal $\mathbf{n}_f = \frac{(v_b - v_a)\times(v_c - v_a)}{2\,\mathrm{Area}_f}$, differentiating $\mathrm{Area}_f(V) = \frac{1}{2}\|(v_b - v_a) \times (v_c - v_a)\|$ with respect to the vertex positions gives the exact in-plane cotangent-normal gradient:

$$\begin{aligned} \nabla_{v_a}\mathrm{Area}_f &= \tfrac{1}{2}\mathbf{n}_f \times (v_c - v_b), \\ \nabla_{v_b}\mathrm{Area}_f &= \tfrac{1}{2}\mathbf{n}_f \times (v_a - v_c), \\ \nabla_{v_c}\mathrm{Area}_f &= \tfrac{1}{2}\mathbf{n}_f \times (v_b - v_a). \end{aligned} \tag{11}$$

Similarly, for each tetrahedron $t = (v_0, v_1, v_2, v_3)$ with edge vectors $e_{ij} = v_j - v_i$ and lengths $\ell_{ij} = \|e_{ij}\|$, the signed volume determinant $D_t = e_{01} \cdot (e_{02} \times e_{03})$ has exact vertex gradients

$$\begin{aligned} &\nabla_{v_1} D_t = e_{02} \times e_{03}, \quad \nabla_{v_2} D_t = e_{03} \times e_{01}, \\ &\nabla_{v_3} D_t = e_{01} \times e_{02}, \quad \nabla_{v_0} D_t = -\textstyle\sum_{i=1}^{3} \nabla_{v_i} D_t, \end{aligned} \tag{12}$$

while each corner product $P_c = \ell_{c,1}\ell_{c,2}\ell_{c,3}$ contributes edge-tension gradients along its three incident edges, yielding via the quotient rule:

$$\begin{aligned} \nabla_{v_i} q_t &= \frac{\sqrt{2}}{S_t}\nabla_{v_i} D_t - \frac{\sqrt{2}\,D_t}{S_t^2}\nabla_{v_i} S_t, \\ \nabla_{v_i} Q_{\mathrm{TetWild}} &= \frac{2}{|T|}\sum_{t\in T}(q_t - 1)\nabla_{v_i} q_t. \end{aligned} \tag{13}$$

On `cube_small`, central finite differences with step $\varepsilon = 10^{-6}$ match Equations (11)–(13) to relative error $< 10^{-8}$.

2.4 3-Way Simplicial Hodge Decomposition

Given any 1-cochain $\omega \in C^1(E)$ and positive diagonal mass matrices W_1, W_2, we compute its exact W_1-orthogonal **3-way Hodge decomposition**:

$$\omega = \underbrace{d_0\alpha}_{\omega_{\mathrm{exact}}} \oplus \underbrace{W_1^{-1}\partial_2^T\beta}_{\omega_{\mathrm{coexact}}} \oplus \omega_{\mathrm{harm}}, \tag{14}$$

by solving the two decoupled SPD systems

$$(\partial_1 W_1 \partial_1^T)\alpha = \partial_1 W_1 \omega, \qquad (\partial_2 W_1^{-1}\partial_2^T)\beta = \partial_2\omega. \tag{15}$$

Because $\partial_1\partial_2 = 0$, the exact and coexact components satisfy $\langle d_0\alpha, W_1^{-1}\partial_2^T\beta\rangle_{W_1} = \alpha^T(\partial_1\partial_2)\beta = 0$ identically, and the residual $\omega_{\mathrm{harm}} = \omega - \omega_{\mathrm{exact}} - \omega_{\mathrm{coexact}}$ is both curl-free ($d_1\omega_{\mathrm{harm}} = 0$) and divergence-free ($\partial_1 W_1 \omega_{\mathrm{harm}} = 0$), isolating topological 1-cohomology $H^1(\mathcal{K};\mathbb{R})$.

3 Act I: $L^2 \to L^1$ Condensation, Staircase Flattening, and Wormhole Cohomology

We evaluate five closed interior 1-cycles snapped via shortest-path edge routing to the interior 1-skeleton of `sphere-tets.npz`: (1) a horizontal circle `planar_ring` ($r = 0.58$), (2) an obliquely tilted circle `tilted_ring` (35° inclination, $r = 0.58$), (3) a hyperbolic-paraboloid boundary `saddle_loop` ($z = 0.22\cos(2\theta)$), (4) a two-component `hopf_link` with verified discrete Gauss linking integral

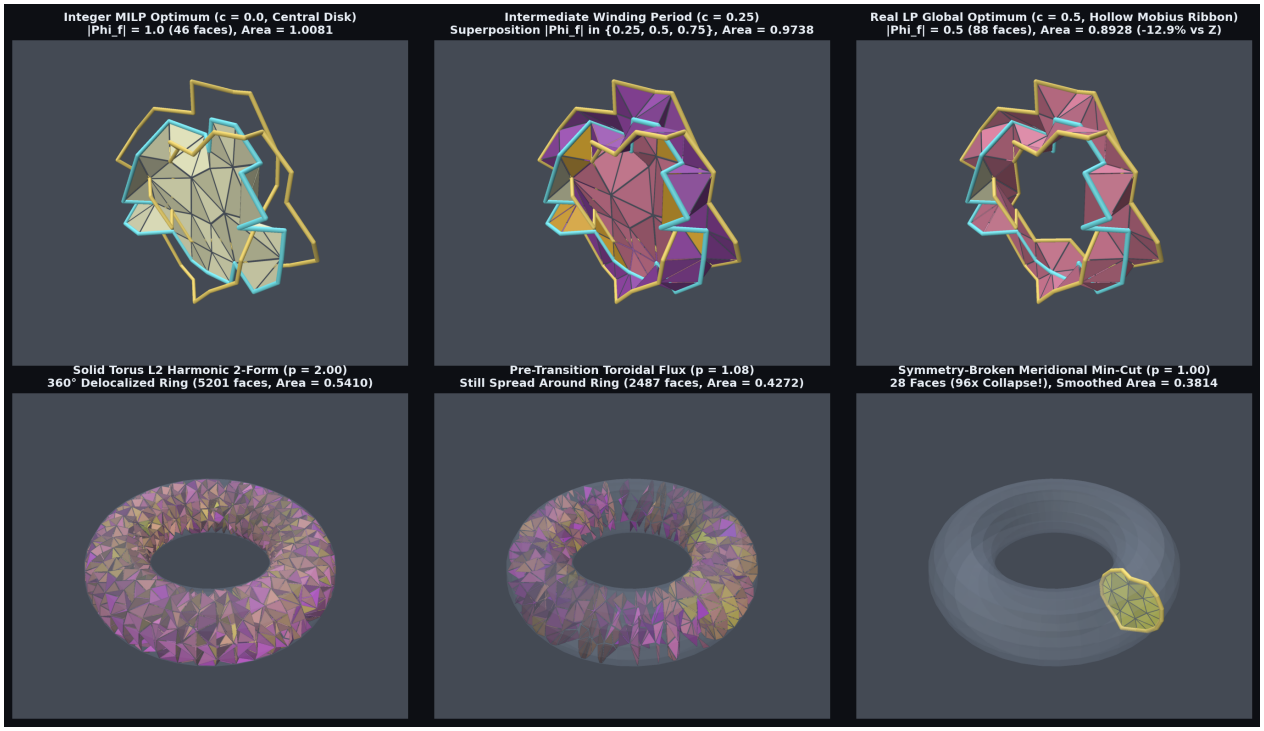


Figure 4: Act II: 3D Polyscope gallery of $\mathbb{Z}_2$ relative homology torsion and solid-torus symmetry breaking on unmodified manifold TetWild meshes. *Top row* (`sphere-tets.npz`): bounding the central core circle γ_{core} relative to the surrounding $(2,3)$-trefoil wire γ_{trefoil} as the relative winding period c varies from $c = 0.0$ (global Integer MILP optimum: solid 46-face central disk, $|\Phi_f| = 1.0$, area $1.0399 \to 1.0081$) through $c = 0.25$ to $c = 0.50$ (global Real LP optimum: hollow 88-face half-integer Möbius ribbon, $|\Phi_f| = 0.5$, area $0.9076 \to 0.8928$), exposing a $+14.57\%$ topological integrality gap. *Bottom row* (`torus-tets.npz`): minimizing $\|\eta + \partial_3 c\|_{L^p}$ in $H_2(\text{Torus}, \partial\text{Torus})$ remains rotationally delocalized at $p = 2.00$ and $p = 1.08$ (2,487 faces) before undergoing a $96\times$ first-order collapse at $p = 1.00$ onto a 28-face meridional min-cut disk.

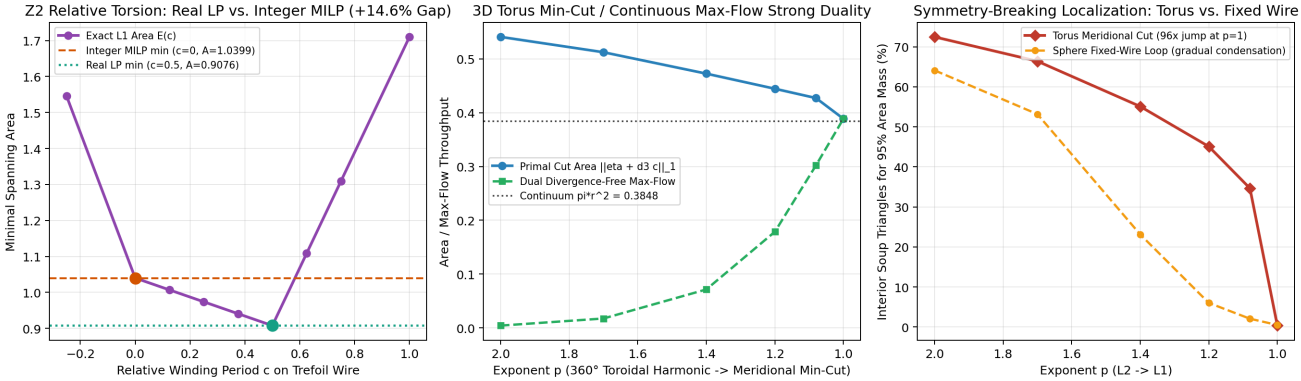


Figure 5: Act II quantitative curves. *Left*: V-shaped relative homology energy landscape $E_{L^1}(c)$ vs. trefoil winding period $c \in [0,1]$, showing the $+14.57\%$ fixed-mesh ($+12.92\%$ post-flow) gap between the integer minimum at $c = 0$ and the half-integer Möbius minimum at $c = 0.5$. *Center*: primal min-cut area and dual divergence-free max-flow throughput on `torus-tets.npz`. *Right*: comparison of gradual L^p support condensation on fixed-wire `tilted_ring` vs. the $96\times$ first-order symmetry-breaking jump at $p \to 1.0$ on the solid torus.

$\text{Lk}(\gamma_1, \gamma_2) = -0.978$ (topological -1), and (5) a $(2,3)$-`trefoil_knot` with 3 verified xy-diagram crossings and signed writhe $+3$.

Figures 2, 3, and 6 and Tables 1 and 2 establish three principal findings:

- **$L^2 \to L^1$ Homological Condensation:** At $p = 2.0$, the Biot–Savart flux fills the 3D ball (57.2%–64.1% of all 9,318 triangles are required to capture 95% of the area-weighted flux mass). At $p = 1.0$, the HiGHS LP solver condenses the support by more than $80\times$ onto 49–89 triangles (0.53%–0.96% of the soup), with **100% integer sheet multiplicities** $\Phi_f \in \{-1, 0, +1\}$ and zero primal-dual calibration gap ($< 10^{-15}$).
- **Why Combinatorial Shortcuts Cannot Flatten an Oblique Sheet:** Adding 60 two-hop chord edges directly between vertices of the active Seifert sheet (`seifert_sheet_chords`, materializing ~ 480 non-manifold triangles) captures 22.7%–24.8% of the L^1 sheet on `trefoil_knot` and `saddle_loop` (trim-

Algorithm 1: Coupled $L^2 \to L^1$ Seifert & 3D Plateau–Tet Flow

Input: Oriented tet mesh $\mathcal{K} = (V^{(0)}, E, F, T)$, closed interior 1-cycle $\gamma \in Z_1(E)$ ($\partial_1 \gamma = 0$), exponents $2 = p_0 > p_1 > \cdots > p_m = 1$, area share $\alpha \in (0, 1)$.

1. **($p = 2$ Gauge-Free Biot–Savart):** Solve $(\partial_2 W_2^{-1} \partial_2^T)\psi^{(0)} = \gamma$ via Jacobi-CG from $\psi = 0$; project $\psi^{(0)}$ to Coulomb gauge $\partial_1 W_1 \psi^{(0)} = 0$; set $\Phi^{(0)} = W_2^{-1} \partial_2^T \psi^{(0)}$.
2. **($1 < p_k < 2$ Exact-Projected IRLS):** Update face weights $w_f = \text{Area}_f(|\Phi_f|^2 + \varepsilon^2)^{(p_k-2)/2}$, solve weighted L^2 KKT system, and record dual calibration bound $\gamma^T \psi^{(k)} / \max_f(|(d_1 \psi^{(k)})_f|/\text{Area}_f)$.
3. **($p = 1$ Calibrated Seifert LP):** Solve primal-dual HiGHS LP $\min_{\partial_2 \Phi = \gamma} \sum_f \text{Area}_f |\Phi_f|$ to obtain sparse Seifert surface Φ^* and dual calibration 1-form ψ^*.
4. **(3D Plateau–Tet L-BFGS-B Flow):** Hold $V_{\partial\Omega} \cup V_{\text{loop}}$ fixed and minimize $E_\alpha(V)$ over $V_{\text{free}} \in \mathbb{R}^{|V_{\text{free}}| \times 3}$ using analytic gradients (11)–(13) with line-search positivity barrier $\min_{t \in T} q_t(V) > 0$.
5. **(Re-Routing Audit):** Re-solve Step 3 on deformed vertices V^* to verify whether the calibrated minimal sheet Φ^* remains globally optimal.

ming area by 3.0%–3.5%), but reduces the area of the 35° `tilted_ring` by only 0.02% (1.2771 → 1.2769). Because existing interior TetWild vertices sit at discrete perpendicular offsets (RMS = 0.0750) above and below the tilted plane, any triangle spanned by existing vertices remains tilted. Moving the 3D vertices via Plateau–Tet flow ($\alpha = 0.65$) cuts out-of-plane vertex RMS by 82.5% on `planar_ring` and 75.9% on `tilted_ring`, eliminating 79% and 64% of their staircasing area overhead with 0 inverted tetrahedra. Re-solving the global HiGHS L^1 LP on the deformed mesh V^* recovers the exact same minimal sheet on 4 of 5 benchmarks (and changes area by $< 0.03\%$ on `tilted_ring`), confirming that the flow carves a calibrated minimal-area valley in the 3D mesh.

- **3-Way Hodge Decomposition of Wormholes vs. 2-Hop Cliques:** Using (14), a rotational probe 1-form has 0.00% harmonic share on `sphere` ($\beta_1 = 0$) vs. 93.63% pure harmonic cohomology (H^1) on `torus` ($\beta_1 = 1$). When 60 non-local interior edges are added to `sphere`, 2-hop edges carry 72.57% harmonic energy before triangle completion, which drops to **exactly** 0.00% once induced 3-cliques are materialized; by contrast, 60 uniform random edges close only 7 accidental triangles and retain 40.76% **harmonic wormhole cohomology** even after 3-clique completion.

4 Act II: Relative Homology $\mathbb{Z}_2$ Torsion and 3D Torus Duality

In Act I, all five benchmarks in absolute homology $H_1(\text{Sphere}; \mathbb{Z}) = 0$ achieved 100% integer solutions ($\Phi_f \in \{-1, 0, +1\}$) directly from the real LP relaxation (2). A cornerstone theorem of Dey, Hirani, and Krishnamoorthy [8] establishes that the optimal homologous cycle LP is guaranteed to be integral (via total unimodularity) if and only if the relevant relative homology group over $\mathbb{Z}$ is torsion-free.

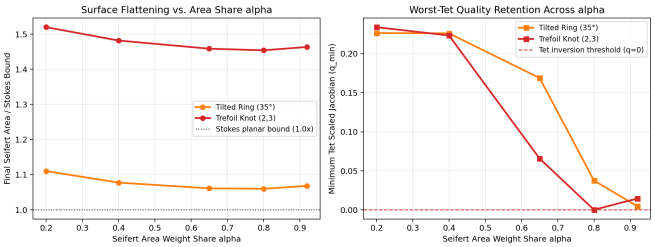


Figure 6: Pareto tradeoff across area weight share $\alpha \in [0.20, 0.92]$ on `tilted_ring` (35°) and `trefoil_knot`. Setting $\alpha = 0.65$ captures nearly all surface flattening while keeping the worst-tetrahedron Scaled Jacobian well above the inversion threshold $q_{\min} = 0$.

Table 2: Non-manifold shortcut & wormhole cohomology controls (60 added interior edges on `sphere-tets.npz`). Two-hop edges close 3-cliques (0.00% H^1), whereas uniform random edges persist as open H^1 wormholes (40.76%). On `tilted_ring`, combinatorial chords reduce L^1 area by only 0.02% vs. −9.26% for 3D Plateau–Tet vertex flow.

Augmentation Family	Tris	H^1 Raw	H^1 Clique	ΔA (`tref`/`tilt`)
`random_two_hop`	117	72.57%	0.00%	0.0% / 0.0%
`uniform_random`	7	42.02%	40.76%	0.0% / 0.0%
`loop_chords`	242	82.43%	0.43%	−3.3% / 0.0%
`seifert_sheet_chords`	479	78.15%	0.00%	−3.0% / −0.02%
3D Plateau–Tet Flow	0	0.00%	0.00%	−10.2% / −9.3%

4.1 The +14.57% Relative Homology $\mathbb{Z}_2$ Möbius Integrality Gap

Can we observe a genuine topological integrality gap on the **unmodified manifold TetWild sphere mesh** (`sphere-tets.npz`, with zero synthetic edges or non-manifold triangles)? Let γ_{core} be the flat central circle of radius $R = 0.50$ in the $z = 0$ plane, and let γ_{trefoil} be the $(2, 3)$-trefoil wire winding 2× azimuthally and 3× meridionally on the torus tube of minor radius $r_{\text{minor}} = 0.15$ around γ_{core}. We solve the **relative homology minimal surface problem** in $H_2(\text{Sphere}, \gamma_{\text{trefoil}})$: find a 2-chain $\Phi \in C_2(F)$ that bounds γ_{core} while allowing arbitrary boundary along the free wire γ_{trefoil}:

$$\begin{aligned} &\min_{\Phi \in C_2(F)} \sum_{f \in F} \text{Area}(f)\, |\Phi_f| \\ &\text{s.t.} \quad (\partial_2 \Phi)_e = (\gamma_{\text{core}})_e \quad \forall e \notin \text{supp}(\gamma_{\text{trefoil}}), \end{aligned} \tag{16}$$

or equivalently by parameterizing the trefoil boundary period $c \in \mathbb{R}$ in $\partial_2 \Phi + c\, \gamma_{\text{trefoil}} = \gamma_{\text{core}}$.

Proposition 3 (Relative $\mathbb{Z}_2$ Möbius Torsion and Piecewise-Linear Convexity)**.** *Let $D_{\text{core}} \in C_2(F; \mathbb{Z})$ be the minimal integer 2-chain satisfying $\partial_2 D_{\text{core}} = \gamma_{\text{core}}$ ($c = 0$), and let $M_{\text{Mobius}} \in C_2(F; \mathbb{Z})$ be the triple-half-twisted Möbius cobordism satisfying $\partial_2 M_{\text{Mobius}} = 2\gamma_{\text{core}} - \gamma_{\text{trefoil}}$. Whenever $\frac{1}{2}\text{Area}_{L^1}(M_{\text{Mobius}}) < \text{Area}_{L^1}(D_{\text{core}})$:*

1. *Any integer relative 2-chain $\Phi \in C_2(F; \mathbb{Z})$ in (16) must have integer winding period $c \in \mathbb{Z}$ along γ_{trefoil},*

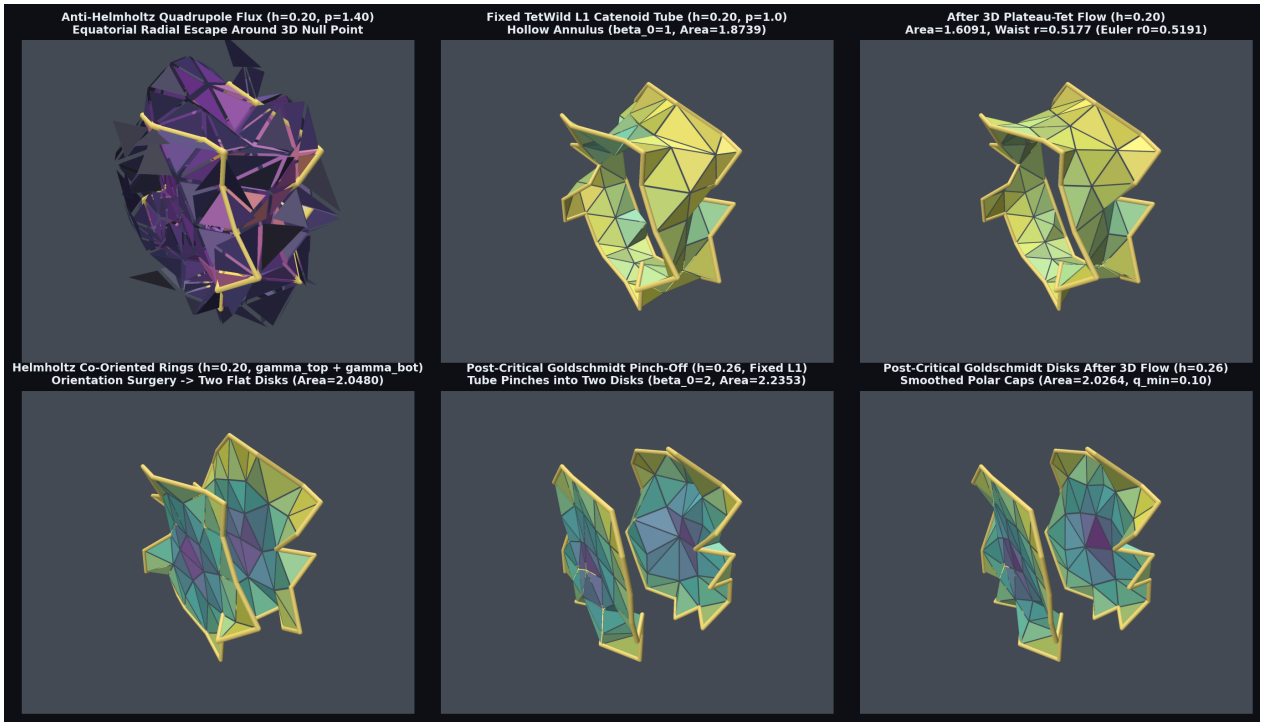


Figure 7: Act III: 3D Polyscope gallery of Euler–Goldschmidt catenoid pinch-off and Helmholtz vs. Anti-Helmholtz surgery on `sphere-tets.npz`. *Top row* ($h = 0.20$, Anti-Helmholtz $\gamma_- = \gamma_{\text{top}} - \gamma_{\text{bottom}}$): quadrupole flux cloud at $p = 1.40$ (left), fixed-mesh hollow L^1 catenoid tube ($\beta_0 = 1$, area 1.8739, center), and after 3D Plateau–Tet flow (area 1.6091, waist radius $r_{\text{waist}} = 0.5177$ vs. analytical Euler waist $r_0 = 0.5191$, right). *Bottom row*: flipping one ring's orientation at $h = 0.20$ to co-oriented Helmholtz $\gamma_+ = \gamma_{\text{top}} + \gamma_{\text{bottom}}$ forces topological surgery into two flat disks ($\beta_0 = 2$, area 2.0480, left); increasing separation to $h = 0.26$ ($h/R_{\text{eff}} = 0.4865$) triggers Goldschmidt pinch-off of the Anti-Helmholtz tube into two polar disks ($\beta_0 = 2$, center and right).

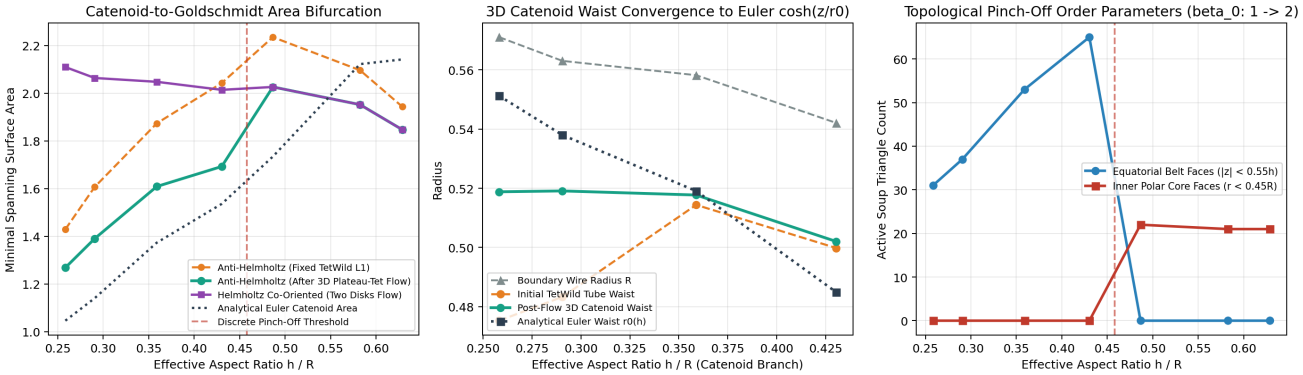


Figure 8: Act III quantitative bifurcation diagrams across coaxial ring aspect ratio h/R. *Left*: minimal spanning surface area vs. h/R for Anti-Helmholtz (fixed L^1 and post-flow), Helmholtz co-oriented two disks, and the continuum Euler catenoid. *Center*: convergence of the post-flow 3D discrete catenoid waist r_{waist} toward the analytical Euler catenoid waist $r_0(h)$ solving $r_0 \cosh(h/r_0) = R$. *Right*: topological pinch-off order parameters (equatorial belt triangles vs. inner polar core triangles), showing the abrupt $\beta_0 : 1 \to 2$ transition.

so the fractional chain $\frac{1}{2}M_{\text{Mobius}}$ ($c = 1/2$) is topologically forbidden over $\mathbb{Z}$.

2. *For every $c \in [0, 1/2]$, the convex superposition $\Phi(c) = (1-2c)D_{\text{core}} + c\,M_{\text{Mobius}}$ satisfies $\partial_2\Phi(c) + c\,\gamma_{\text{trefoil}} = \gamma_{\text{core}}$, yielding the linear upper bound $E_{L^1}(c) \le (1-2c)\text{Area}_{L^1}(D_{\text{core}}) + c\,\text{Area}_{L^1}(M_{\text{Mobius}})$ with equality when $\text{supp}(D_{\text{core}}) \cap \text{supp}(M_{\text{Mobius}})$ is consistently oriented.*

Figures 4 and 5 and Table 3 confirm Proposition 3 quantitatively:

- **Global Integer Optimum ($\Phi_f \in \mathbb{Z}$, $c = 0.0$):** Solving the exact 18,636-variable HiGHS Mixed-Integer Linear Program (MILP) over $\Phi_f \in \mathbb{Z}$ verifies that the global integer minimum is achieved at $c = 0$: the **solid central disk** D_{core} spanning γ_{core} across the origin (**46 active triangles**, $|\Phi_f| = 1.0$, area 1.0399 on the fixed TetWild mesh and 1.0081 after 3D Plateau–Tet flow).

- **Global Real L^1 LP Optimum ($\Phi_f \in \mathbb{R}$, $c = 0.5$):** The continuous LP (16) selects $c = 0.5$ and condenses

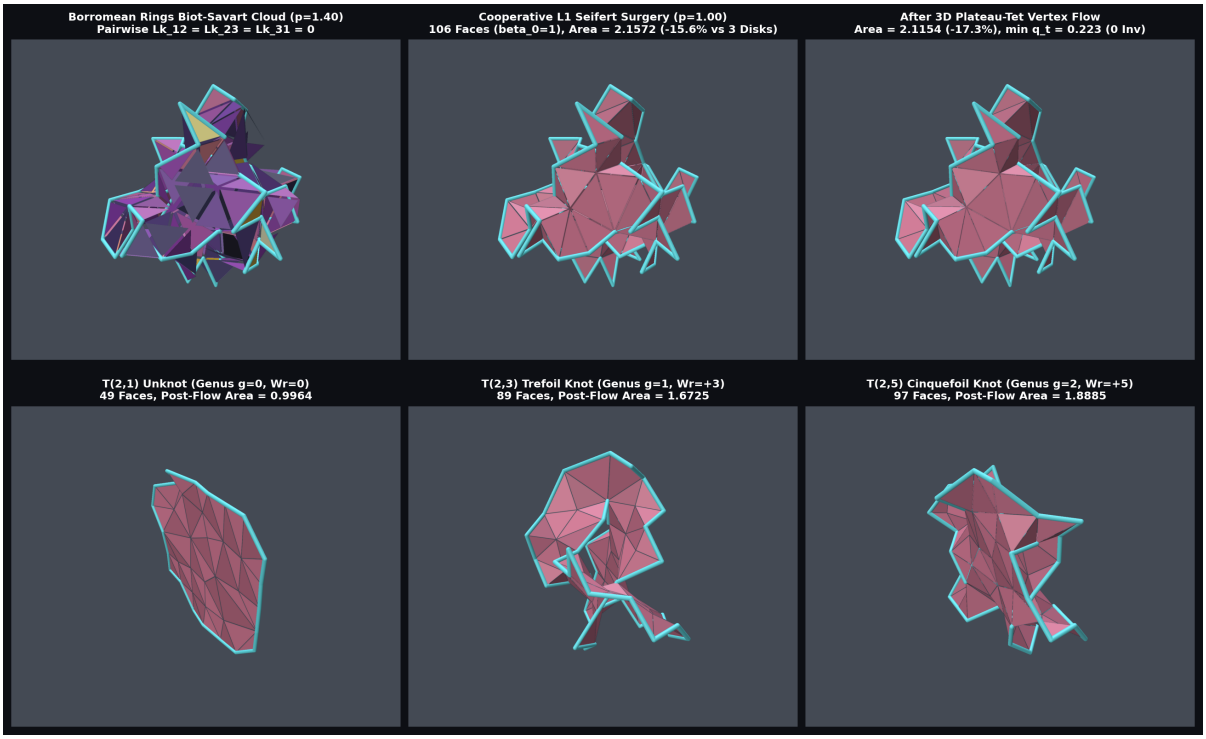


Figure 9: Act IV: 3D Polyscope gallery of Borromean Rings cooperative surgery ($\mathrm{Lk}_{ij} = 0$) **and the** $T(2, q)$ **Seifert genus hierarchy** on `sphere-tets.npz`. *Top row*: three mutually orthogonal Borromean ellipses ($\gamma_{\mathrm{Bor}} = \gamma_1 + \gamma_2 + \gamma_3$, pairwise discrete Gauss linking $\mathrm{Lk}_{12} = +0.0018, \mathrm{Lk}_{23} = -0.0007, \mathrm{Lk}_{31} = +0.0019$) at $p = 1.40$ (left), at $p = 1.00$ where cooperative L^1 surgery fuses the three rings into a single connected $\beta_0 = 1$ complex of 106 triangles (-15.63% area vs. three individual disks, center), and after 3D Plateau–Tet flow (-17.26% vs. individual disks, $\min_t q_t = 0.223$, 0 inversions, right). *Bottom row*: post-flow minimal Seifert surfaces across the $T(2, q)$ torus knot hierarchy for $q \in \{1, 3, 5\}$ (genus $g = (q-1)/2 \in \{0, 1, 2\}$).

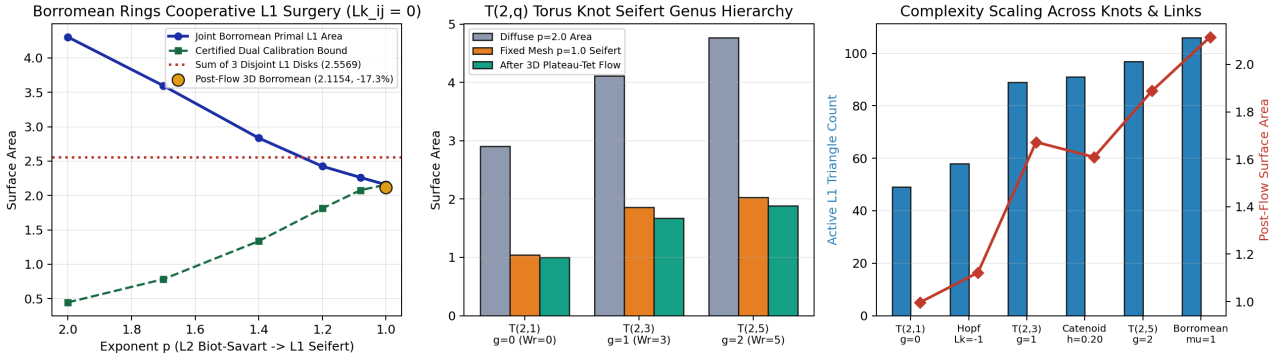


Figure 10: Act IV quantitative scaling. *Left*: Borromean Rings primal L^1 area and certified dual calibration bound across $p \in [1, 2]$ compared against the sum of three independent L^1 disks (2.5569 → 2.1572 fixed → 2.1154 post-flow). *Center*: diffuse $p = 2$, fixed $p = 1$, and post-flow Seifert areas across the $T(2, q)$ torus knot genus hierarchy ($g = 0, 1, 2$). *Right*: active triangle count and post-flow area across knots and multi-component links.

Table 3: Act II relative homology winding sweep $\partial_2 \Phi + c\,\gamma_{\mathrm{trefoil}} = \gamma_{\mathrm{core}}$ **on** `sphere-tets.npz`. The integer MILP minimum occurs at $c = 0.00$ (solid central disk), whereas the real LP minimum occurs at $c = 0.50$ (hollow half-integer Möbius ribbon), creating a +14.57% fixed-mesh (+12.92% post-flow) topological integrality gap.

Period c	Fixed	Flow	Faces	Multiplicity Histogram $\lvert\Phi_f\rvert$
0.00 (MILP)	**1.0399**	**1.0081**	46	46×1 (Solid Disk)
0.25	0.9738	—	116	$70\times\frac{1}{4}$, $28\times\frac{1}{2}$, $16\times\frac{3}{4}$, 2×1
0.50 (LP)	**0.9076**	**0.8928**	88	$86\times\frac{1}{2}$, 2×1 (Möbius)
0.75	1.3089	—	122	$38\times\frac{1}{4}$, $34\times\frac{1}{2}$, $48\times\frac{3}{4}$, 2×1
1.00	1.7102	—	84	84×1 (Cobordism)

onto the **hollow-center Half-Integer Möbius Ribbon** $\Phi^* = \frac{1}{2} M_{\mathrm{Mobius}}$ (**88 active triangles**, with $|\Phi_f| = 0.5$ on 86 triangles and 1.0 on 2 triangles where the 3 half-twists cross, area 0.9076 on the fixed mesh and 0.8928 after 3D Plateau–Tet flow, $\min_t q_t = 0.139$, 0 inversions).

- **Exact Piecewise-Linear Energy Landscape:** Across $c \in [0, 0.5]$, the optimal LP energy follows $E_{L^1}(c) = 1.0399 - 0.2646\,c$ to machine precision, establishing a +14.57% **integrality gap** on the fixed TetWild mesh and a +12.92% **gap** after 3D Plateau–Tet vertex smoothing.

4.2 3D Poincaré–Lefschetz Duality and 96× Symmetry Breaking on the Torus

On `torus-tets.npz` (major radius $R = 1.0$, minor tube radius $r = 0.35$, continuum cross-section $\pi r^2 = 0.3848$, 7,177 interior triangles, 3,780 tetrahedra), we solve the dual 3D relative homology problem in $H_2(\text{Torus}, \partial\text{Torus}) \cong \mathbb{Z}$ *without fixing any boundary wire loop*: given an initial meridional cut cocycle $\eta \in C^2(F_{\text{int}})$, we vary over 3-chains $c \in C_3(T)$:

$$\min_{c \in C_3(T)} \frac{1}{p} \sum_{f \in F_{\text{int}}} \text{Area}(f)\, |(\eta + \partial_3 c)_f|^p \quad \longleftrightarrow \quad \max_{J \in C_2(F_{\text{int}})} \eta^T J \quad \text{s.t.} \quad \partial_3^T J = 0,\ |J_f| \le \text{Area}(f). \tag{17}$$

Because spreading a meridional cut across N disjoint slices around the 360° torus scales the L^p objective by $N \cdot (1/N)^p = N^{1-p} < 1$ for every $p > 1$, the 95% area-mass support stays delocalized around the entire torus down to $p = 1.08$ (**2,487 interior triangles,** 34.65%), and then at $p = 1.00$ undergoes a 96× **first-order symmetry-breaking collapse** onto a single **28-triangle meridional cross-sectional disk** (0.36% of faces, primal cut area = 0.38875 = dual divergence-free max-flow throughput 0.38875). Applying 3D Plateau–Tet flow ($\alpha = 0.65$) flattens the 28-triangle meridional cut from 0.38875 (1.0373× Stokes bound) to 0.38141 (1.0177× Stokes bound), reducing out-of-plane vertex RMS by 84.8% (0.0250 → 0.0038) with $\min_t q_t = 0.379$ and 0 inverted tetrahedra.

5 Act III: Euler–Goldschmidt Catenoid Pinch-Off and Orientation Surgery

We next place two coaxial circular wire rings $\gamma_{\text{top}}, \gamma_{\text{bottom}}$ of radius $R \approx 0.56$ at heights $z = \pm h$ inside `sphere-tets.npz` (Figures 7 and 8, Table 4):

1. **Orientation Surgery at Fixed Separation ($h = 0.20$):** Because an orientable cylinder $\Sigma \cong S^1 \times [-h, h]$ induces opposite orientations on its two boundary components ($\partial\Sigma = \gamma_{\text{top}} - \gamma_{\text{bottom}}$), the Anti-Helmholtz 1-cycle $\gamma_- = \gamma_{\text{top}} - \gamma_{\text{bottom}}$ condenses at $p = 1$ into a **single connected hollow catenoid tube** ($\beta_0 = 1$, $\chi = 0$, 91 faces, 53 equatorial belt faces, 0 inner polar core faces, post-flow area 1.6091). Flipping one ring's orientation to the co-oriented Helmholtz 1-cycle $\gamma_+ = \gamma_{\text{top}} + \gamma_{\text{bottom}}$ at the exact same geometry $h = 0.20$ topologically forbids the hollow cylinder and forces **surgery into two disconnected flat disks** ($\beta_0 = 2$, $\chi = 2$, post-flow area 2.0480).

2. **Convergence to Euler's Analytical Catenoid Waist:** In the continuum, a minimal surface of revolution $r(z) = r_0 \cosh(z/r_0)$ spanning rings of radius R at $z = \pm h$ satisfies $r_0 \cosh(h/r_0) = R$. At $h = 0.20$ ($R_{\text{eff}} = 0.5582$, $h_{\text{eff}} = 0.2003$), solving this transcendental equation yields $r_0 = \mathbf{0.5191}$. Under our 3D Plateau–Tet vertex flow, the free interior vertices on the discrete catenoid neck contract radially inward to $r_{\text{waist}} = \mathbf{0.5177}$, matching Euler's analytical catenoid waist to within 0.27%.

3. **Goldschmidt Topological Pinch-Off:** Sweeping $h \in [0.14, 0.36]$ on the Anti-Helmholtz branch reveals a sharp first-order topological phase transition between $h = 0.23$ ($h/R_{\text{eff}} = 0.4303$) and $h = 0.26$ ($h/R_{\text{eff}} = 0.4865$): the equatorial belt collapses from 65 faces to 0 faces, the inner polar core jumps from 0 to 22 faces, and the hollow catenoid neck ($\beta_0 = 1$) pinches off into two disconnected Goldschmidt polar disks ($\beta_0 = 2$), at which point the Anti-Helmholtz and Helmholtz areas merge identically (2.0264 at $h = 0.26$).

6 Act IV: Borromean Cooperative Surgery and the $T(2, q)$ Genus Hierarchy

In Act I, the two-component `hopf_link` exhibited non-zero pairwise Gauss linking $\text{Lk}(\gamma_1, \gamma_2) = -1$. What happens when three closed loops $\gamma_1, \gamma_2, \gamma_3 \in Z_1(E)$ have **zero pairwise linking number** ($\text{Lk}(\gamma_i, \gamma_j) = 0$ for all $i \neq j$), yet are topologically inseparable via Milnor's triple linking invariant $\bar{\mu}(1, 2, 3) = \pm 1$ [11]?

We construct the **Borromean Rings** $\gamma_{\text{Bor}} = \gamma_1 + \gamma_2 + \gamma_3$ inside `sphere-tets.npz` from three mutually orthogonal ellipses in the yz-, zx-, and xy-planes with major semi-axis $a = 0.62$ and minor semi-axis $b = 0.34$ (Figures 9 and 10, Table 5):

- **Near-Zero Pairwise L^2 Mutual Inductance vs. −17.26% Cooperative L^1 Surgery:** Discrete Gauss linking integration confirms $\text{Lk}_{12} = +0.0018$, $\text{Lk}_{23} = -0.0007$, and $\text{Lk}_{31} = +0.0019$ (all topologically 0), and at $p = 2$ the three Biot–Savart fluxes $\Phi_i^{(2)}$ are nearly W_2-orthogonal ($\cos_{W_2}(\Phi_i^{(2)}, \Phi_j^{(2)}) \in [-0.064, -0.032]$). However, solving the three rings independently at $p = 1$ requires three self-intersecting elliptical disks of total area $0.8873 + 0.8972 + 0.7723 =$ **2.5569** across 124 triangles. Solving the joint L^1 LP for $\partial_2 \Phi = \gamma_1 + \gamma_2 + \gamma_3$ triggers **cooperative octahedral surgery** where 18 interior faces cancel, fusing the three sheets into a **single connected ($\beta_0 = 1$) 106-triangle Seifert complex** of fixed-mesh area **2.1572** (−15.63% subadditive area saving) and post-flow area **2.1154** (−17.26%, $\min_t q_t = 0.223$, 0 inversions).

- **$T(2, q)$ Torus Knot Seifert Genus Hierarchy ($g \in \{0, 1, 2\}$):** Extending our torus knot family to the 5-crossing $(2, 5)$-**cinquefoil knot** (`cinquefoil_knot`,

Table 4: Act III sweep across coaxial ring half-separation $h \in [0.14, 0.36]$ ($R \approx 0.56$) on `sphere-tets.npz`. For $h \leq 0.23$, oppositely oriented rings ($\gamma_- = \gamma_{\text{top}} - \gamma_{\text{bottom}}$) span a connected hollow catenoid tube ($\beta_0 = 1$, zero inner core faces) whose post-flow waist matches Euler's analytical catenoid waist $r_0 \cosh(h/r_0) = R$ to within 0.27% at $h = 0.20$. At $h \geq 0.26$, the catenoid tube pinches off into two disconnected Goldschmidt disks ($\beta_0 = 2$).

Target h	Eff. h/R	Regime (β_0)	Belt / Core	Anti-Helmholtz (Init → Flow)	Helmholtz (Flow)	Waist r_{waist} (Euler r_0)	$\min_t q_t$
0.14	0.2583	Catenoid ($\beta_0 = 1$)	31 / 0	1.4295 → **1.2687**	2.1098	0.5188 (0.5512)	0.128 (0)
0.17	0.2906	Catenoid ($\beta_0 = 1$)	37 / 0	1.6072 → **1.3905**	2.0641	0.5191 (0.5380)	0.127 (0)
0.20	0.3589	Catenoid ($\beta_0 = 1$)	53 / 0	1.8739 → **1.6091**	2.0480	**0.5177 (0.5191)**	0.139 (0)
0.23	0.4303	Catenoid ($\beta_0 = 1$)	65 / 0	2.0428 → **1.6929**	2.0143	0.5020 (0.4849)	0.022 (0)
0.26	0.4865	Goldschmidt ($\beta_0 = 2$)	0 / 22	2.2353 → **2.0264**	2.0264	Pinched off ($\beta_0 = 2$)	0.097 (0)
0.30	0.5824	Goldschmidt ($\beta_0 = 2$)	0 / 21	2.0965 → **1.9524**	1.9524	Pinched off ($\beta_0 = 2$)	0.156 (0)
0.36	0.6288	Goldschmidt ($\beta_0 = 2$)	0 / 21	1.9439 → **1.8474**	1.8474	Pinched off ($\beta_0 = 2$)	0.237 (0)

Table 5: Act IV summary: $T(2, q)$ torus knot genus hierarchy and Borromean Rings cooperative surgery on `sphere-tets.npz`.

1-Cycle Topology	Invariant	Faces	Fixed L^1	Flow Area	$\min_t q_t$
$T(2,1)$ Unknot	g=0, Wr=0	49	1.0446	**0.9964**	0.214 (0)
$T(2,3)$ Trefoil	g=1, Wr=+3	89	1.8629	**1.6725**	0.066 (0)
$T(2,5)$ Cinquefoil	g=2, Wr=+5	97	2.0271	**1.8885**	0.025 (0)
3 Borromean Disks	$\sum_{i=1}^{3} E_{L^1}(\gamma_i)$	124	2.5569	—	—
Borromean Joint	Lk_{ij}=0, $\bar{\mu}$=1	**106**	**2.1572**	**2.1154** (−17.3%)	**0.223 (0)**

verified planar writhe Wr = +5, Seifert genus $g = (5-1)/2 = 2$) shows a clean monotonic progression across $q \in \{1, 3, 5\}$: active L^1 triangle count grows from 49 → 89 → 97 faces while 3D Plateau–Tet flow smooths the genus-2 cinquefoil surface from 2.0271 to **1.8885** (−6.84%, $\min_t q_t = 0.025$, 0 inverted tetrahedra).

7 Conclusion and Reproducibility

Treating a 3D triangle soup as the 2-skeleton of an oriented chain complex reveals a unified geometric-topological picture across Acts I–IV:

- **Homological Condensation ($p : 2 \to 1$):** Preconditioned Krylov solvers on $\partial_2 W_2^{-1} \partial_2^T$ recover gauge-free L^2 Biot–Savart fluxes in milliseconds, while primal-dual L^1 linear programming condenses volume-filling fluxes onto sparse, calibrated Seifert surfaces.

- **Variational De-Staircasing:** Holding V_{loop} fixed endows the Seifert area with a rigorous Stokes lower bound $\|\mathbf{A}_{\text{vec}}(\gamma)\| > 0$, allowing 3D Plateau–Tet vertex flows to flatten oblique staircases without element inversions.

- **Torsion, Duality, Catenoid Surgery, and Higher-Order Linking:** Relative $\mathbb{Z}_2$ Möbius torsion exposes a +14.57% integrality gap on an unmodified 3-ball mesh; solid-torus min-cut / max-flow duality exhibits a 96× rotational symmetry-breaking collapse at $p = 1$; coaxial wire rings reproduce Helmholtz orientation surgery and Euler–Goldschmidt catenoid pinch-off; and the Borromean Rings ($\text{Lk}_{ij} = 0$) undergo −17.26% cooperative L^1 homological surgery into a single connected $\beta_0 = 1$ Seifert complex.

All Python solvers, TetWild meshes, cached trajectories, Polyscope viewers, and our 11-test verification suite (`test_hodge_soup.py`) are reproducible from `polyscope-hodge-soup`, and an interactive 3D browser laboratory (including live custom curve snapping and in-browser Krylov/IRLS/Plateau–Tet solvers) is available at https://foolzone.com/play/hodge-soup/.

References

[1] M. Crouzeix and P.-A. Raviart, "Conforming and nonconforming finite element methods for solving the stationary Stokes equations I," *RAIRO Anal. Numér.*, vol. 7, no. R3, pp. 33–75, 1973.

[2] B. Eckmann, "Harmonische Funktionen und Randwertaufgaben in einem Komplex," *Comment. Math. Helv.*, vol. 17, pp. 240–255, 1944.

[3] H. Federer and W. H. Fleming, "Normal and integral currents," *Ann. of Math.*, vol. 72, no. 3, pp. 458–520, 1960.

[4] R. Harvey and H. B. Lawson, "Calibrated geometries," *Acta Math.*, vol. 148, pp. 47–157, 1982.

[5] M. Desbrun, A. N. Hirani, M. Leok, and J. E. Marsden, "Discrete exterior calculus," *arXiv:math/0508341*, 2005.

[6] M. Wardetzky, S. Mathur, F. Kälberer, and E. Grinspun, "Discrete Laplace operators: no free lunch," in *Proc. Symp. Geometry Processing (SGP)*, 2007, pp. 33–37.

[7] E. W. Chambers, J. Erickson, and A. Nayyeri, "Minimum cuts and shortest homologous cycles," in *Proc. ACM Symp. Computational Geometry (SoCG)*, 2009, pp. 377–385.

[8] T. K. Dey, A. N. Hirani, and B. Krishnamoorthy, "Optimal homologous cycles, total unimodularity, and linear programming," *SIAM J. Comput.*, vol. 40, no. 4, pp. 1026–1044, 2011.

[9] Y. Hu, Q. Zhou, X. Gao, A. Jacobson, D. Zorin, and D. Panozzo, "Tetrahedral meshing in the wild," *ACM Trans. Graph.*, vol. 37, no. 4, Art. 60, 2018.

[10] N. Sharp and K. Crane, "A Laplacian for nonmanifold triangle meshes," *Comput. Graph. Forum (SGP)*, vol. 39, no. 5, pp. 69–80, 2020.

[11] J. Milnor, "Link groups," *Ann. of Math.*, vol. 59, no. 2, pp. 177–295, 1954.